2.2 Recent Progress on Understanding and Quantifying Atom Probe Tomography Artifacts for High Evaporation Rate nm-scale Phases in Fe Based Alloys

— P. Wells, N. J. Cunningham and G. R. Odette (University of California Santa Barbara)

OBJECTIVE

Atom probe tomography (APT) is a key technique for characterizing the small Y-Ti-O nano-oxides in nanostructured ferritic alloys (NFAs). The objective of this study is to address composition discrepancies between TEM measurements and APT, focusing on APT artifacts.

SUMMARY

Preferential undercounting and trajectory aberrations in APT measurements were investigated. The higher than physical atom densities observed in NFs are due to trajectory aberrations that are associated with local changes in the surface topology of the tip of the AP needle that focus both solute and matrix atoms into a smaller detector area. These topology changes are due to higher evaporation rates of the solutes and, in some cases, nearby matrix atoms that cause flattening or dimpling of the tip at the nano-oxides. The rapid evaporation rates are also accompanied by multiple hits and/or pre-evaporation events that can lead to undercounting of some solute species. These measurement artifacts are amplified in reconstructions that do not take them into account, for example, by placing atoms actually evaporated from a lower layer in a surface position. These phenomena are well known to APT practitioners, but their implications have not been widely recognized or well treated. However, atom probe data sets contain information that can provide insight on these phenomena, and perhaps eventually contribute to their resolution. A key piece of information is the spatially resolved sequence of atom emissions that are visualized in reconstruction software in color-coded detector hit maps. The hit maps show that the nano-oxides (and Cu rich precipitates in a ferrite matrix) evaporate much more rapidly than randomly located matrix atoms, and focus into the center of the solute rich region. Matrix atoms near the nano-oxides evaporate even more rapidly and focus more intensely than the solutes. Simple volume conservation considerations dictate that the higher evaporation rates lead to changes in the tip morphology resulting in the trajectory aberrations. Crude estimates of the degree of flattening-dimpling are possible, but more detailed understanding of the tip shape evolution will require additional observations and integration with field emission and atomic bond energy models. The hit maps also reveal that when the surface of a tip approaches a NF the thin layer of matrix atoms between the NF and the tip surface rapidly evaporates, forming a pre-dimple. Hit maps also show that un-ranged detector noise is concentrated at the nano-oxides, possibly partly due to DC pre-emission or unresolved multiple hit events. Solute specific multiple event frequencies are presented and other artifacts, like nano-oxide tops and bottoms, are described.

PROGRESS AND STATUS

Introduction and Background

Nano-structured ferritic alloys (NFA) have high tensile and creep strength permitting operation up to 800°C, manifest remarkable resistance to radiation damage and can manage a high concentration of He [1]. These outstanding properties derive from an ultrahigh density of Y-Ti-O enriched nano-features (NF) that provide dispersion strengthening, help stabilize dislocation and

fine grain structures, reduce excess concentrations of displacement defects and trap He in fine bubbles [1]. The NF size, number density, and composition have been the focus of recent research on numerous alloys including MA957 [2,3,4]. A detailed understanding of the NF is needed since the number density and size distribution govern the geometric sink strength, while the NF-matrix interface is critical to defect and He trapping, dislocation pinning-detachment processes and the thermal and irradiation stability. Further, detailed knowledge about the effects of compositional and processing variables that control the NF character is critical to the design of alloys with an optimal balance of properties.

Characterization of the NFs is difficult due to their small sizes that are near the resolution limit of many experimental techniques. Therefore, characterization with a complementary set of state of the art tools is needed to mitigate the limitations of individual methods. Two core characterization tools used in this research include APT and TEM. Conventional bright-field TEM resolves all but the smallest NFs by contrast differences with the matrix, but other TEM techniques are required for determining their structure and composition. These include high angle annular dark field (HAADF) imaging, electron energy loss spectroscopy (EELS), energy dispersive x-ray spectroscopy (EDS) and high resolution TEM (HRTEM). The larger (>15 nm) Y-Ti-O rich features appear to be either Y_2TiO_5 or $Y_2Ti_2O_7$ [5,6,7,8]. Most TEM studies have shown that the smallest NFs (≤ 5 nm) in MA957 are near stoichiometric $Y_2Ti_2O_7$ [6,7,8,9,10,11,12], although both non-stoichiometric rock salt and amorphous NF structures have been reported [13,14]. A recently initiated collaboration between UCSB, UCB and LBNL using the advanced aberration corrected TEAM 0.5 microscope at the LBNL National Electron Microscopy Center has shown the NFs in MA957 are primarily coherent $Y_2Ti_2O_7$ [15].

Atom probe tomography (ATP) was the first technique used to study the smallest NFs (≤ 5 nm) [16,17] and APT continues to be a major tool used to characterize NFAs. APT and TEM NF number densities and size distributions are generally in good agreement especially considering the individual limitations of both techniques [18,19]. However, standard interpretations of APT data suggest the NFs are far from equilibrium, coherent, transition phase (sub-oxide) solute clusters with lower Y/Ti and O/(Ti + Y) ratios compared to $Y_2Ti_2O_7$ [16,17,18,19]. For example, the average specimen Y/Ti ratio of the NFs in MA957 measured at UCSB using a Cameca 3000X HR LEAP and IVAS reconstruction software ranged from 0.27 to 0.46. The corresponding average O/(Y + Ti) ratio ranged from 0.63 to 0.80. The IVAS APT reconstructions also show very high Fe and Cr contents of ≈ 50 to 75 % even in the center of small NFs. We believe the inconsistency between $Y_2Ti_2O_7$ versus these compositions is in large part due to artifacts in the APT method [20,21,22]. The artifacts include DC pre-emission and unresolved multiple hits of more weakly bonded species like Y and O [15,20], surface diffusion, especially interstitial elements like O, perhaps stimulated by the high electric fields, and the presence of nearby low index pole zones. Further, structures like precipitate-matrix interfaces, isolated surface atoms versus those on ledges and ledge kinks and uneven temperature distributions during the laser pulsing may also lead to large local variations in the binding energies and field emission evaporation rates.

However, perhaps the most important APT artifacts are due to differences in the evaporation fields and/or the electric fields of second phase particles and the evaporation fields for the matrix atoms. Differences in local evaporation rates directly affect the local topology of the APT needle tip. While this issue has long been recognized it has not been dealt with in an effective and quantitative way. However, a recent study by Oberdorfer and G. Schmitz that simulated local lower evaporation fields and higher electric fields associated with more weakly bonded phases

and dielectric phases like oxides, respectively, showed more rapid evaporation and flattening or dimpling of the region in the vicinity of the feature [23]. This results in topology induced ion trajectory aberrations due to the change in the local magnification factor. Both solute and matrix atoms are focused into the center of the precipitate region. Such trajectory aberrations are signaled by a higher than physical atom density near the center of the precipitates as well as artificially high concentrations of matrix atom (Fe and Cr). A recent unpublished simulation we have seen also shows that dimpling not only leads to a focusing effect, but it can actually result in crossovers in the ion trajectories that further complicate reliable reconstructions.

Coupled with assumptions used in the reconstruction algorithms and sometimes imprecise calibration of d-spacings, these artifacts also lead to distortion of the shapes of second phase particles (flattening and elongation) as well as features with chemically segregated tops and bottoms in some cases (when there are no physical tops and bottoms along the APT axial z-direction) and even large shifts in the location of the constituents in a binary alloy feature [24].

This work focuses on the mechanisms responsible for the APT-TEM composition discrepancy with TEM associated with preferential ion species undercounting and trajectory aberrations.

Experimental Procedures

APT is a destructive microscopy method that identifies the position and species of atoms within sharp needle samples with tip diameters of 100 nm or less. Feature numbers, sizes, compositions and spatial compositional variations were measured in NFA MA957 using a Cameca 3000X HR LEAP instrument with a variety of experimental conditions including sample temperatures between 30 and 70 K using both 200 or 250 kHz laser and voltage pulse modes and a 20-25% voltage pulse fraction or laser energies from 0.05 to 0. 5 nJ. Reconstructions and analysis of the 3-dimenstional data was performed using the Imago Interactive Visualization and Analysis Software (IVAS) package.

Precipitates were identified and their composition measured using the maximum separation distance method for the solute ions of interest, namely Y, Ti and O, including their complex forms like TiO and YO [25,26]. One-dimensional composition and density profiles through the NFs and larger precipitates were used to observe and compare the atom distributions perpendicular (X and Y directions) and parallel (Z direction) to the tip axis.

The evaporation sequence was also investigated using so-called detector hit maps and by analyzing the multiple hits on the detector during a single voltage or laser pulse. The mass to charge ratio of the field-emitted species is determined by the time of flight between the voltage, or laser, pulse that causes the ion to evaporate and when it hits the detector. The ions are field evaporated at a rate determined by the temperature as well as the standing bias and pulse voltages. The position the atoms hit the detector (X_d, Y_d) is used in conjunction with reconstruction software to determine the corresponding atom (X, Y) position on the tip based on its curvature defining a focal point assumed to be determined by the radius of an ideal hemisphere. The tip is then eroded by an increment of DZ for each hit that depends on the atomic volume of the evaporated species and the detector efficiency. Thus each detected ion is associated with an X, Y and Z position in the reconstruction. In the case of pure metals it is possible to reconstruct the atomic planes and plane d-spacing's; and using deviations from nominal d-spacings to adjust the reconstruction parameters so that they are consistent. In the case of a pure metal or the matrix of a phase-separated system, the evaporation rates and

sequence vary with the distance to the center of a faceted planar pole and by the field evaporation statistics and local arrangement of surface atoms.

However, the situation is much more complex for phase separated regions on an alloy since the evaporation field varies between the atomic/ionic species and its local environment that effectively determine its binding energy to the surface [27,28]. First we will digress to discuss the much studied and debated Fe-Cu system. One example of profound effects of the species and local environment is the evaporation of Cu atoms dissolved in a Fe matrix. Bulk Cu has a lower bulk evaporation field than Fe (30 vs 33 V/nm). However, the differences in evaporation fields are magnified when the Cu is dissolved in Fe, since the Fe-Fe and Cu-Cu bonds are much stronger than the Fe-Cu bonds. Thus Cu is preferentially evaporated at a higher rate than Fe. Indeed this effect is so strong that at higher temperatures most of the Cu pre-evaporates between laser or voltage pulses. For example in one study the ratio of the measured Cu to bulk Cu decreases from about 1 at 50°K to 0.2 at 120 °K [29]. We have observed similar effect in a simple Fe-Cu-Mn alloy containing both dissolved Cu and Cu precipitates. Note the 3kT/2 energy difference between 60 and 120°K is equivalent to only ≈ 0.0075 eV. Such small differences are comparable to or less than excess energies associated with atoms in a bcc versus fcc crystal structure, at interfaces, associated with defects and subject to coherency strains. Even ignoring pre-evaporation, higher local field emission of atoms from a second phase particle lead to the changes in local topology noted above, resulting in flattening or dimpling of the tip surface (which is any event not an ideal hemisphere) that produces trajectory aberrations. Further, as noted above the electric fields are higher at a non-conducting dielectric phase like an oxide, also leading to enhanced evaporation and local flattening or dimpling. These concepts are schematically illustrated in Figure 1. While these phenomena have been recognized for some time, current reconstruction algorithms do not take pre-emission, surface diffusion, preferential evaporation or trajectory aberrations into account.

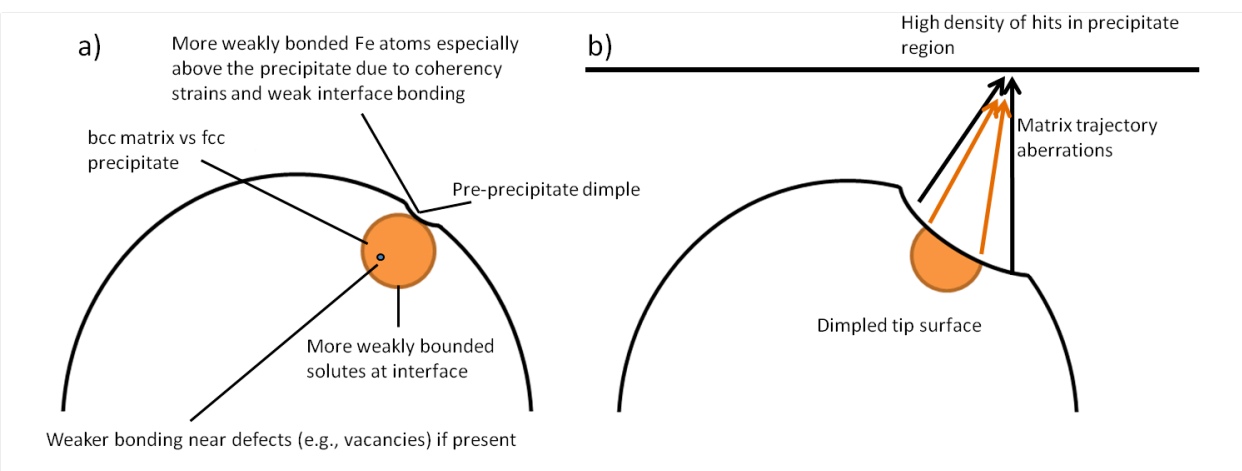

Figure 1. a) Tip showing concepts of strain effects and weak interface bonds before a precipitate is encountered that cause a pre-precipitate dimple. b) Dimpling of tip caused by evaporation of higher field precipitate leading to Fe trajectory aberrations.

RESULTS

Hit Map Analysis

Considerable insight and ultimately perhaps some degree of quantification and resolution of these issues can be obtained by examining the spatially correlated sequence of emissions that are now currently available in the IVAS software. IVAS also provides information from the detector that is then used to create a visualization of the spatially dependent evaporation rates in the form of color-coded hit maps (HM) for the individual species. An example of a typical HM is shown in Figure 2. This HM is taken from an irradiated pressure vessel steel that contains a high density of Cu-Mn-Ni precipitates. This sample was run on our LEAP 3000X HR in voltage mode at 60K and 15% pulse fraction. Here the tip surface has been divided into X-Y bins roughly ≈ 1 nm in size. The color-coding shows the number of either matrix Fe atoms (Figure 2a and c) or solute atoms (Figure 2b and d). The atom hits are binned at each point for a range of about 20,000 atoms. Figures 2a and b show the emissions before the precipitate is encountered. These HM also clearly show that the matrix Fe atoms (Fig. 2a) above the actual precipitates preferentially evaporate, probably due to a combination of weaker local bonding and coherency stains. This creates a pre-dimple even before the precipitate emerges at the tip (Fig. 2b). Figures 2c and d show the corresponding HM in the precipitate itself, demonstrating that the matrix Fe atoms are focused into the precipitate region (bright red spot in Figure 2c) along with the solute atoms (the light blue spot in Figure 2d).

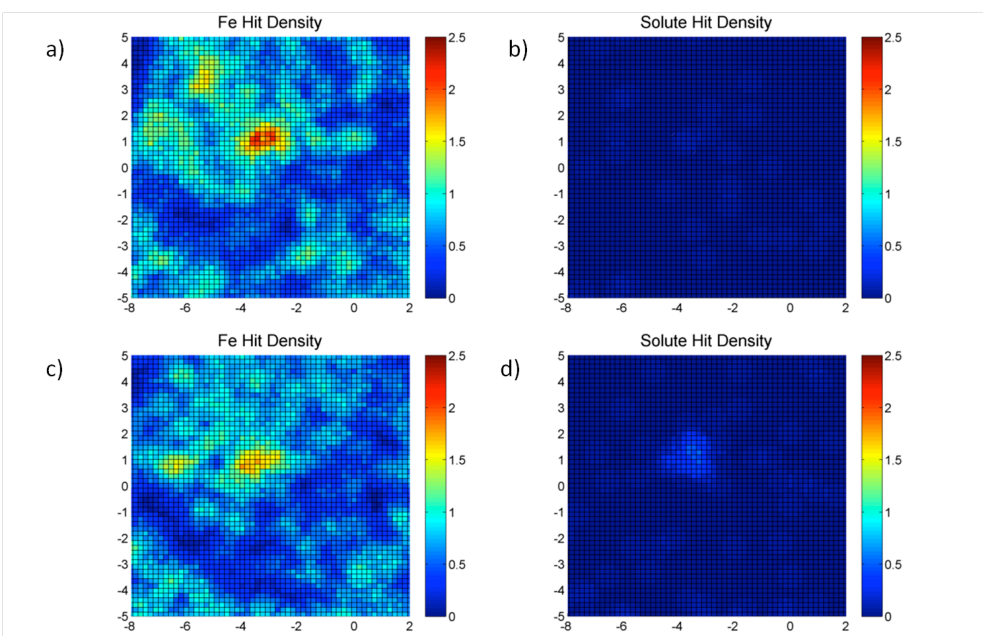

Figure 2. a-b) HM showing hits before the precipitate is uncovered for a) Fe, b) solutes; c-d) HM showing hits during precipitate evaporation for c) Fe and d) solute.

Figure 3a and b shows another HM of the spatial distribution of the Fe and Ni in a region with a Cu-Ni-Mn precipitate. Figure 3c shows the HM distribution of the HM noise that is defined as the un-ranged ions that form the background in the charge to mass spectrum shown in Figure 3d. The spatial correlation of the HM for noise with that for the precipitate presumably arises from a pre-evaporation event, or evaporation of atoms between voltage or laser pulses, making it impossible to determine the time of flight of the incoming atom. It is not possible to distinguish between the different elements that make up the noise, but the fact that it is highly localized in the precipitate region and given that pre-emission and multiples are biased for more weakly bonded atoms (see below) it seems likely that the localized noise partially rationalizes the differences in the APT vs TEM in the solute content as well.

The number of excess Fe atom hits above the precipitates suggests that the pre-dimple could be up to 4 or 5 atom layers. However, because the dimpling effect also leads to matrix trajectory aberrations, it is difficult to discriminate the relative contributions of pre-dimpling the Fe above the precipitate versus trajectory aberration contributions from the surrounding Fe matrix. That is the dimple may be shallow and larger in diameter or deeper and smaller in diameter. More quantitative treatment of these phenomena are summarized in the future work section.

Figure 4 and 5 show similar phenomena occur in the Fe-Cr matrix containing nano-oxide precipitates. Again preferential matrix atom evaporation takes place before the nano-oxide is encountered forming a pre-dimple (Figs. 4a and b). Trajectory aberrations of solutes and matrix atoms are observed as the precipitate evaporates (Figs. 4c and d). A spatially correlated increase in noise at the nano-oxide location is also observed (Fig. 5). Thus pre-emission and multiples may rationalize the low Y/Ti ratios.

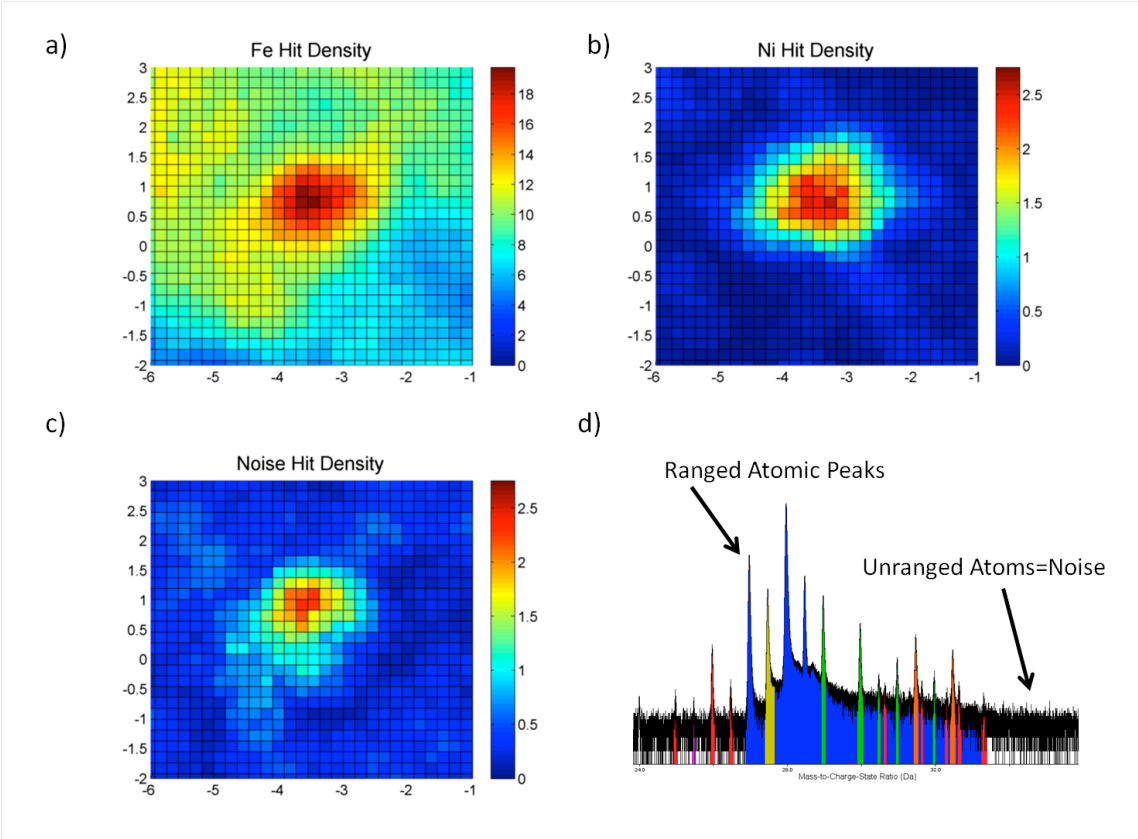

Figure 3. a-b) HM showing hits during precipitate evaporation for a) Fe, b) solutes and c) noise. Note the different scales between figures a versus b & c, d) the mass spectrum is shown is to clarify the meaning of noise.

Atom Densities and Possible Feature Shape and Composition Distribution Artifacts

Figure 6 shows a much higher density in the nano-oxide compared to the matrix, indicating the presence of trajectory aberrations. The trajectory aberrations coupled with the reconstruction algorithm assumptions produce nano-oxides shapes with either high or low aspect ratios in the Z vs X-Y directions, depending on the size of the nano-oxide (or precipitate). The smallest nano-oxides (≈ 2-3 nm diameter) appear compressed in the Z direction whereas the larger nano-oxides appear elongated in the Z direction as shown in the examples in Figure 7. Once the precipitate is exposed on the tip surface it quickly evaporates and the reconstruction algorithm places the solutes artificially high in the Z direction. For larger precipitates that take longer to evaporate the trajectory aberrations may focus the precipitate ions more narrowly in the x-y direction perhaps elongating the nano-oxides.

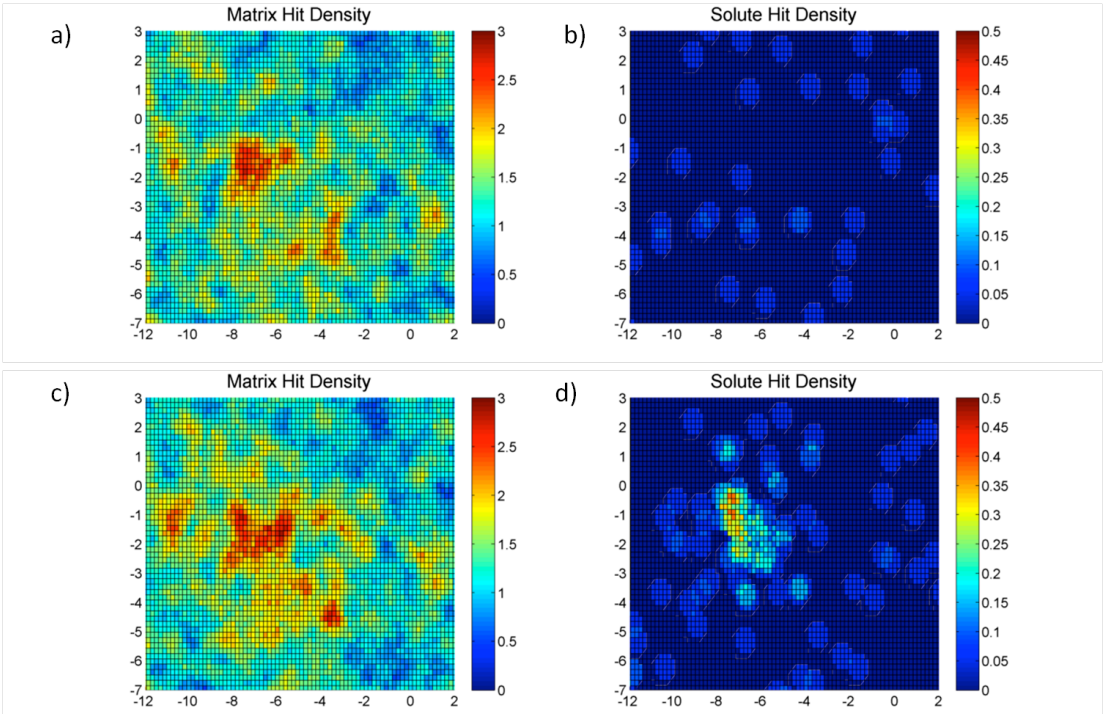

Figure 4. a-b) HM showing hits before the precipitate is uncovered for a) Fe+Cr, b) solutes; c-d) HM showing hits during precipitate evaporation for c) Fe+Cr and d) solutes. Note scale difference between matrix atom (a and c) and solute atoms (b and d).

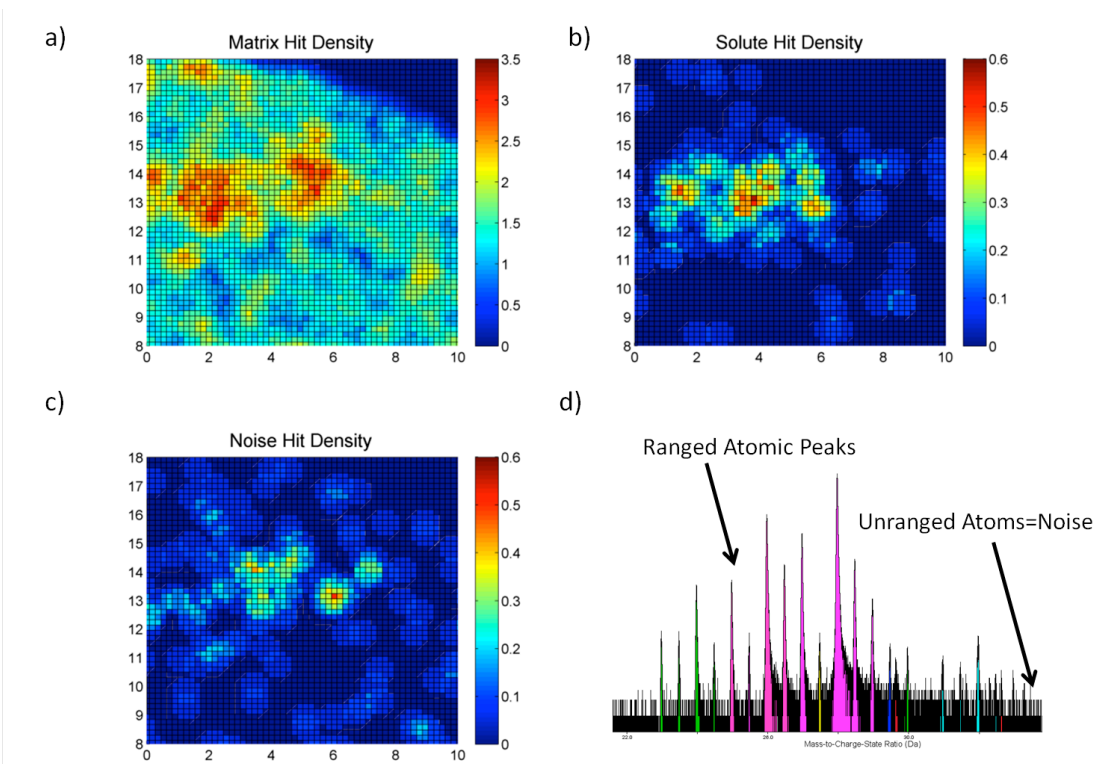

Figure 5. HM showing hits during precipitate evaporation for a) Fe+Cr, b) solutes and c) noise. The mass spectrum is shown to clarify the definition of noise. Note the scale difference between figures a, b & c.

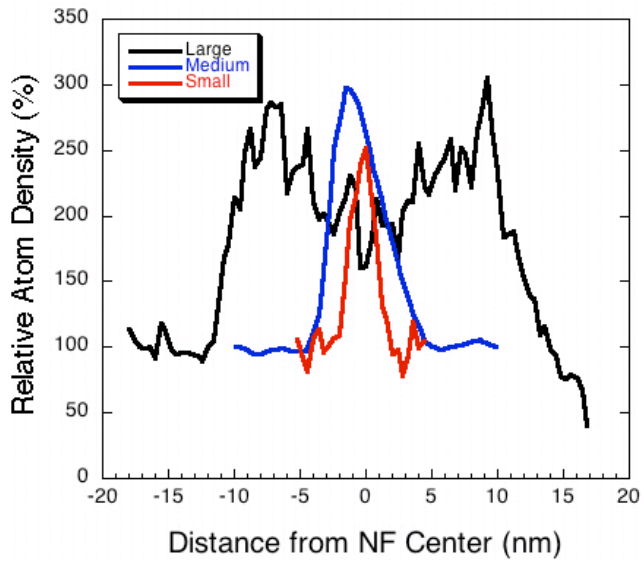

Figure 6. One-dimensional Z direction profile through a large, medium and small nano-oxide showing higher atom density compared to the matrix.

Another artifact is shown in the one-dimensional composition profiles of Figure 7 for a large, medim and small precipitate where a high concentration of TiO ions occurs near the bottom of the oxide and a small elemental Ti peak is observed at the top. Since the precipitates would not have "tops" and "bottoms" this is obviously an APT artifact. The ion distribution is more symmetric in the X-Y direction as seen in Figure 7b for the large precipitate.

The low APT Y/Ti ratio could in principle be due to excess Ti segregation in the ferrite matrix adjacent to the nano-oxide. Assuming a $Y_2Ti_2O_7$ structure and using the Y count gives the equivalent spherical size shown in Table 1 for the nano-oxides in Figure 7. The excess Ti is also given. Assuming this excess is due to 100% Ti segregation to the NF-matrix interface the required layer thickness, also given in Table 1, is only the order of one or two atoms assuming a TiO (cubic) structure. If these interface Ti atoms evaporate at a higher field than the nano-oxide solutes, trajectory aberrations could place them inside the NF volume. After the NF is removed, remnants of the Ti segregation could evaporate more slowly producing the TiO tails seen in the reconstructions.

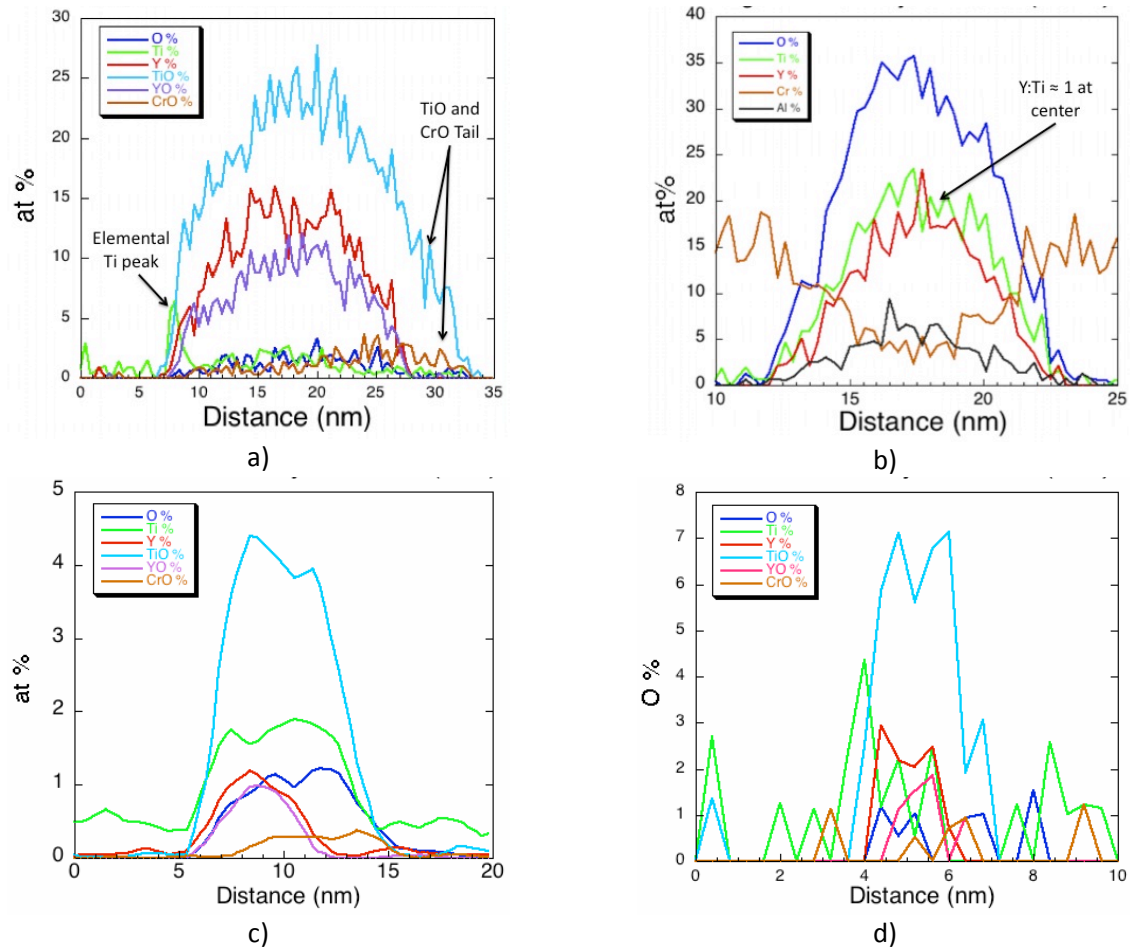

Figure 7. One-dimensional composition profiles of a) large NF along z direction; b) large NF perpendicular to z-direction; c) medium NF along z direction; and d) small NF along z direction.

Table 1. Calculated diameter based on assumed $Y_2Ti_2O_7$ structure and Y count with required Ti segregation volume thickness to account for the excess Ti.

NF	$Y_2Ti_2O_7$ Diameter (nm)	Segregated Ti thickness (nm)
Large N_Y = 5,429, N_{Ti} = 8,289	12.16	0.29
Medium N_Y = 174 N_{Ti} = 659	3.8	0.18
Small N_Y = 35 N_{Ti} = 125	2.4	0.23

Another possible explanation for the low Y/Ti ratio is preferential undercounting due to pre-emissions and multiple detector events. Multiple ions removed during a single voltage or laser pulse are still resolved by the delay line detector as long as they are not of the same species. If they are the same species and hit the detector too closely together in time, then they are not counted since their exact position cannot be determined. Since the nano-oxide solutes evaporate rapidly from the same area on the tip then they may be preferentially undercounted, especially if they evaporate more often in pairs. Table 2 shows the percent of atoms counted during a multiple event for a typical MA957 tip. Oxygen has the highest multiple ion evaporation rate of 74%. YO ions follow at 64% and Y and TiO at 47% and 49%, respectively. In contrast, only 2% of the Fe ions involve multiples events. The issue of multiples need further analysis, but it is noted that the Y emissions are almost entirely from the nano-oxides.

Table 2. Percent of atoms evaporated during a multiple event.

Fe	Cr	CrO	Ti	TiO	Y	YO	O
2.0	5.5	74.0	6.6	48.5	46.8	64.2	74.4

CONCLUSIONS

We believe that the composition differences in Y-Ti-O nano-oxides observed by APT and TEM are at least partly due to a combination of trajectory aberrations and solute under counts due to pre-emission and unresolved multiples. Our hypothesis is that the excess Fe content in nano-oxides is primarily caused by trajectory aberrations caused by local flattening or dimpling of the tip due to preferential evaporation due to a higher local electric field near the dielectric phase and perhaps more weakly bound solutes. Analysis of HM shows that matrix directly above the precipitate is also preferentially evaporated, probably due to weaker interfacial bonds and coherency strain effects, creating a pre-dimple even before the precipitate is reached. Differences in Y/Ti ratio can be explained with two hypotheses. The first is that Y atoms could be preferentially undercounted due to pre-evaporation and/or because of unresolved multiple events. We assume that pre-emission of an element produces a uniform background noise in the mass spectrum. HM show a large increase in noise focused in the precipitate region during precipitate evaporation. Y and YO evaporate as multiples over 50% of the time. However, much more work needs to be done to confirm that preferential undercounting is indeed happening. A second hypothesis regarding the Y/Ti ratio is that there could be a Ti shell around the nano-oxides that is not detected by TEM methods since it might be only a few atom layers thick. The combination of APT measurement artifacts and reconstruction assumptions can also lead to distortion of the nano-oxide shapes and composition distribution artifacts.

FUTURE RESEARCH

Future work will be directed at observing the topology of the tip using high resolution TEM and FIM methods. We will also carry out additional analysis of the solute specific and spatially correlated emission sequences and integrate this information with simulations of field emission. For example, we are collaborating with Cameca in their simulations of low evaporation field precipitates. These simulations include precipitates with core shell structures with different evaporation fields that are aimed at, for example, understanding chemically segregated tops and bottoms. These simulations will also show the evolution of the local surface topology and the

corresponding trajectory aberrations. This information will be combined with the empirical quantitative emission sequence assessments to develop a more robust approach to APT reconstructions. Further, we will carry out systematic measurements of the evaporation time-temperature kinetics and link this information to atomistic simulations of atomic bonding energies.

REFERENCES

[1] G. R. Odette, M. J. Alinger, and B. D. Wirth, Annual Review of Materials Research, Vol. **38**, 2008, 472.

[2] Y. Wu, E. Haney, N. Cunningham and G. R. Odette, submitted to Acta Mater 2010; under review.

[3] A. Etienne, N. J. Cunningham, Y. Wu, et al., *Mat. Sci. & Tech*. 2011; 27-4:724.

[4] N. J. Cunningham, G. R. Odette, E. Stergar, E. A. Marquis, A. Etienne, C. Hatzoglou, B. Radiguet, and P. Pareige, "Inter-Laboratory Atom Probe Tomography Characterization Study of the Nanofeatures and the Bulk and Matrix Compositions of US MA957," DOE Fusion Reactor Materials Program Semiannual Report, Vol. **50**, 2011, 41-46. DOE/ER-0313/50.

[5] R. Kasada, N. Toda, K. Yutani, H. S. Cho, H. Kishimoto, and A. Kimura, *J. Nucl. Mater.,* **367-370** (2007) 222-228.

[6] H. Sakasegawa, L. Chaffron, F. Legendre, L. Boulanger, T. Cozzika, M. Brocq, and Y. de Carlan, *J. Nucl. Mater.,* **284** (2009) 115-118.

[7] S. Yamashita, N. Akasaka, and S. Ohnuki, *J. Nucl. Mater.* **329-333** (2004) 377-381.

[8] M. Klimienkau, R. Lindau, and A. Moslang, *Micron* **36** (2005) 1-8.

[9] M. Klimienkau, R. Lindau, and A. Moslang, *J. Nucl. Mater,* **329-333** (2004) 347-351.

[10] M. C. Brandes, L. Kovarik, M. K. Miller and M. J. Mills, *J. Mater. Sci.* (2012) 47:3913.

[11] J. Ribis and Y. de Carlan, *Acta Materialia* (2012) 60:238.

[12] A. Hirata, T. Fujita, Y. R. Wen, J. H. Schneibel, C. T. Liu and M. W. Chen, *Nature Mater.* (2011) 10:922.

[13] M. C. Brandes, L. Kovarik, M. K. Miller and M. J. Mills, *J. Mater. Sci. (*2012) 47:3913.

[14] A. Hirata, T. Fujita, Y. R. Wen, et al., *Nature Mater.* (2011) 10:922.

[15] J. Ciston, Y. Wu, G. R. Odette and P. Hosemann, "The Structure of Nanoscale Precipitates and Precipitate Interfaces in an Oxide Dispersion Strengthened Steel," Fusion Materials Semiannual Progress Report for the Period Ending December 31, 2011, DOE-ER-0313/51;2012: in press.

[16] M. K. Miller, D.T. Hoelzer, E. A. Kenik, K. F. Russell, *J. Nucl. Mater.* **329-333** (2004) 338-341.

[17] M. K. Miller, D. T. Hoelzer, E. A. Kenik, and K. F. Russell, *Intermetallics* **13** (2005) 387-392.

[18] N. J. Cunningham, G. R. Odette, and E. Stergar, "Further Atom Probe Tomography Studies of Nanostructured Ferritic Alloy MA957 in Three Conditions," DOE Fusion Reactor Materials Program Semiannual Report, Vol. **49**, 2010, 11-16. DOE/ER-0313/49.

[19] N. J. Cunningham, A. Etienne, Y. Wu, E. M. Haney, and G. R. Odette, "On the Oxide Nanofeatures and Precipitates in the Nano-Structured Ferritic Alloy MA957: A Multiple Technique Study of Heat to Heat Variations and the Effects of Friction Stir Welding and Long Term Thermal Aging," DOE Fusion Reactor Materials Program Semiannual Report, Vol. **48**, 2010, 60-67. DEO/ER-0313/48.

[20] E. A. Marquis and J. Hyde, *Mater. Sci. Eng.* (2010) 69:37.

[21] E. A. Marquis, *Appl. Phys. Lett*. (2008) 93:181904.

[22] C. A. Williams, E. A. Marquis, A. Cerezo and G. D. W. Smith, *J. Nucl. Mater*. (2010) 400:37.

[23] C. Oberdorfer and G. Schmitz, *Microsc. Microanal*. (2011) 17:15.

[24] E. A. Marquis and F. Vurpillot, *Microsc. Microanal*. **14** (2008) 561.

[25] D. Vaumousse, A. Cerezo, P. J. Warren, *Ultramicroscop,* **95** (2003) 215.

[26] J. M. Hyde, C. A. English, G. E. Lucas, M. A. Kirk Jr., R. G. Elliman (Eds.), Proc. of the MRS 2000 Fall Meeting, Symp. R: Microstructural Processes in Irradiated Materials 650, Materials Research Society (2000/2001) R6.6.1.

[27] F. Vurpillot, A. Bostel, and D. Blavette, *App. Phys. Lett.* (2000) 76:3127.

[28] B. Gault, M. P. Moody, F. de Geuser, D. Haley, L. T. Stephenson, and S. P. Ringer, *App. Phys. Lett.* (2009) 95:034103.

[29] Y. Yamaguchi, J. Takahashi, and K. Kawakami, *Ultramicroscopy* **109** (2009) 541-544.